

# Confluence of theory and experiment reveals the catalytic mechanism of the Varkud satellite ribozyme

Abir Ganguly<sup>1,2,7</sup>, Benjamin P. Weissman<sup>3,7</sup>, Timothy J. Giese<sup>1,2</sup>, Nan-Sheng Li<sup>4</sup>, Shuichi Hoshika<sup>5</sup>, Saieesh Rao<sup>3</sup>, Steven A. Benner<sup>5</sup>, Joseph A. Piccirilli<sup>3,4\*</sup> and Darrin M. York<sup>1,2,6\*</sup>

**The Varkud satellite ribozyme catalyses site-specific RNA cleavage and ligation, and serves as an important model system to understand RNA catalysis. Here, we combine stereospecific phosphorothioate substitution, precision nucleobase mutation and linear free-energy relationship measurements with molecular dynamics, molecular solvation theory and ab initio quantum mechanical/molecular mechanical free-energy simulations to gain insight into the catalysis. Through this confluence of theory and experiment, we unify the existing body of structural and functional data to unveil the catalytic mechanism in unprecedented detail, including the degree of proton transfer in the transition state. Further, we provide evidence for a critical Mg<sup>2+</sup> in the active site that interacts with the scissile phosphate and anchors the general base guanine in position for nucleophile activation. This novel role for Mg<sup>2+</sup> adds to the diversity of known catalytic RNA strategies and unifies functional features observed in the Varkud satellite, hairpin and hammerhead ribozyme classes.**

The remarkable ability of RNA molecules to catalyse complex chemical transformations has profoundly influenced our understanding of the role of RNA in biology, the design of new biotechnology and the formulation of theories into the origin of life itself<sup>1,2</sup>. From a chemistry perspective, it is of fundamental interest to understand how RNA, with its limited repertoire of fairly inert functional groups, can achieve rate enhancements typically up to six orders of magnitude or more<sup>3</sup>, in some cases comparable to the intrinsic rates of protein enzymes<sup>4</sup>. A predictive understanding of catalytic RNA mechanisms may enable general principles to emerge that are transferable to the design of synthetic systems, such as the recently reported hachimoji DNA/RNA (ref. <sup>5</sup>), with great promise for new biotechnological applications. In-depth studies of self-cleaving ribozymes, of which there are currently nine known classes, have contributed substantially to our understanding of these mechanisms<sup>6,7</sup>.

The Varkud satellite (VS) ribozyme is the largest known self-cleaving ribozyme, and among the largest endonucleolytic ribozymes (only certain RNase P constructs are comparable). It is found in the mitochondria of natural isolates of *Neurospora* and performs site-specific scission of multimeric VS RNAs into linear monomers<sup>8,9</sup>. Since its discovery nearly three decades ago, the VS ribozyme has been the subject of numerous experimental studies that have provided tremendous insight into its structural and functional properties. The ribozyme cleavage proceeds in a fashion similar to that observed in other self-cleaving ribozymes, through nucleophilic attack of a 2'-hydroxy on the scissile phosphate to form 2',3'-cyclic phosphate and 5'-hydroxy termini (Fig. 1). Electrophoretic mobility and Förster resonance energy transfer (FRET) studies<sup>10,11</sup> have led to models for the VS tertiary structure, and mutagenesis and chemical

probing studies, along with pH-rate measurements<sup>11-14</sup>, have identified residues critical for activity. A significant body of functional data suggests that two critical active-site nucleobases, G638 and A756, act as general base and acid, respectively, in the reaction<sup>11-18</sup> (Fig. 1). It has been established that Mg<sup>2+</sup> ions stabilize the VS ribozyme structure, but the specific catalytic role of Mg<sup>2+</sup> in the active site has not previously been determined.

Despite the abundance of functional data available for the VS ribozyme, in the absence of an atomic-resolution structure, its active-site architecture and key catalytic interactions have remained elusive. Recently, we reported the first pre-catalytic high-resolution crystal structures of the VS ribozyme, the G638A (PDB ID 4R4V) and A756G (PDB ID 4R4P) mutants, by introducing a C634G mutation that facilitated the remodelling and binding of the substrate helix (ref. <sup>19</sup>). In a follow up study, we crystallized the G638A mutant (PDB ID 5V3I) without the C634G mutation and demonstrated that the substrate helix can remodel itself naturally during the course of binding<sup>20</sup>. These structures revealed the complex interlacing of the different helices that give rise to the dimeric, domain-swapped structure of the ribozyme, and were largely consistent with the existing body of VS ribozyme literature<sup>21,22</sup>. Although these structures provide meaningful insight into the global architecture of the ribozyme, they represent only average structures of artificially deactivated catalysts in a crystal, which may not be representative of the dynamic active state in solution. Moreover, these structures were obtained in the presence of high ammonium ion concentrations, which may preclude divalent metal ion binding. As a consequence, major gaps exist in our understanding of the active-site architecture and the catalytic mechanism. Here, we take an integrated experimental and computational approach to establish a dynamic model

<sup>1</sup>Laboratory for Biomolecular Simulation Research, Rutgers, The State University of New Jersey, Piscataway, NJ, USA. <sup>2</sup>Institute for Quantitative Biomedicine, Rutgers, The State University of New Jersey, Piscataway, NJ, USA. <sup>3</sup>Department of Chemistry, The University of Chicago, Chicago, IL, USA. <sup>4</sup>Department of Biochemistry and Molecular Biology, The University of Chicago, Chicago, IL, USA. <sup>5</sup>Foundation for Applied Molecular Evolution, Firebird Biomolecular Sciences, Alachua, FL, USA. <sup>6</sup>Department of Chemistry and Chemical Biology, Rutgers, The State University of New Jersey, Piscataway, NJ, USA. <sup>7</sup>These authors contributed equally: Abir Ganguly, Benjamin P. Weissman. \*e-mail: [jpiccir@uchicago.edu](mailto:jpiccir@uchicago.edu); [Darrin.York@rutgers.edu](mailto:Darrin.York@rutgers.edu)

of VS catalysis that extends and unifies the existing body of experimental data, defines the catalytic configuration and reveals the modes of transition-state stabilization unambiguously. These findings broaden our mechanistic understanding of the diverse array of catalytic strategies available to RNA.

Here, we performed a series of computational and experimental investigations on the VS ribozyme to characterize its functionally active state, identify its key catalytic strategies and unify the existing body of structural and functional data on this important system. We adopted a recently developed ontology for the discussion of RNA cleavage reactions<sup>23</sup>, extended from the original framework introduced by Breaker and co-workers<sup>24</sup>, specifically,  $\alpha$  catalysis, the acquirement of in-line nucleophilic attack,  $\beta$  catalysis, the stabilization of negative charge on non-bridging phosphoryl oxygens (NPOs),  $\gamma$  catalysis, the activation (deprotonation) of the 2'-hydroxy group to generate the nucleophile, and  $\delta$  catalysis, the stabilization of the negative charge on the 5'-oxygen of the leaving group (Fig. 1). The results are divided into eight sections. In the first section, mutational analysis of the catalytic nucleobases A756 and G638 in the background of oxo and phosphorothioate substrates reveals a stereospecific functional linkage between the exocyclic amines of both residues and the pro- $R_p$  NPO of the scissile phosphate. In section two, molecular dynamics (MD) simulations departing independently from each of the three existing crystal structures (none of which contained a  $Mg^{2+}$  in the active site) collectively converge to an ensemble that is reflective of a catalytically inactive state of the ribozyme. In section three, MD simulations and calculations based on molecular solvation theory predict a  $Mg^{2+}$  binding pocket at the pro- $S_p$  NPO position of the scissile phosphate (not yet observed crystallographically). In section four, the predicted  $Mg^{2+}$ -bound model is verified by stereospecific thio/metal-ion rescue effect experiments. In section five, MD simulations with a  $Mg^{2+}$  at the pro- $S_p$  position converge to an ensemble that is reflective of the active state of the ribozyme and illustrate that the metal ion organizes the active site for catalysis in a way that appears to be unique to VS. In section six, chemically precise mutational experiments further validate the  $Mg^{2+}$ -bound model and probe interactions in the metal ion binding pocket. In section seven, linear free-energy relationship (LFER) analysis provides insight into the nature of the rate-controlling transition state, and in particular, the degree of proton transfer for the general base and acid. In section eight, ab initio quantum mechanical/molecular mechanical (QM/MM) free-energy simulations departing from the  $Mg^{2+}$ -bound model reveal a concerted mechanism for RNA backbone cleavage with a late transition state for the cleavage reaction with extensive/complete proton transfer from the 2'-hydroxy to G638, but only partial proton transfer from A756 to the 5'O leaving group, consistent with the LFER analysis. Taken together, the integrated experimental and theoretical data provide detailed atomic-level insight into the catalytic mechanism of the VS ribozyme. These results establish new functional connections between VS and both the hammerhead and hairpin ribozymes, and identify a novel role for a divalent metal ion in organizing the active site by anchoring the general base guanine and tuning its  $pK_a$  to promote general base catalysis ( $\gamma$  catalysis).

## Results

**Phosphorothioate substitution and mutational analysis of A756 and G638 reveal catalytic interactions in the active site.** In this section, we use stereospecific phosphorothioate substitution and chemically precise nucleobase modifications to pinpoint key functional interactions between the pro- $R_p$  position of the substrate scissile phosphate and A756 and G638 in the active site. The results are summarized in Table 1 (further details are provided in the Supplementary Information). Building on earlier work by others<sup>25,26</sup>, our stereospecific phosphorothioate substitution experiments indicated that under standard conditions (10 mM  $MgCl_2$ , 25 mM KCl,

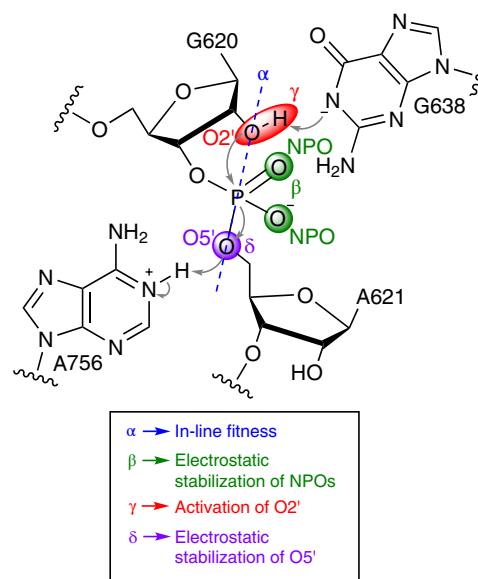


**Fig. 1 | Schematic illustration of the VS ribozyme catalytic reaction.**

The ribozyme catalyses site-specific phosphodiester cleavage by using a guanine, G638, and an adenine, A756, as a general base and acid, respectively. The key catalytic strategies employed by ribozymes<sup>23</sup> are highlighted:  $\alpha$  corresponds to the acquirement of in-line nucleophilic attack (blue),  $\beta$  to the neutralization of negative charge on NPOs (green),  $\gamma$  to the deprotonation of the 2'-hydroxy group to activate the nucleophile (red) and  $\delta$  to the neutralization of the negative charge on the 5'O leaving group (purple).

2 mM spermidine, pH=8), the wild-type (WT) ribozyme cleaved with  $k_{obs} = 0.32 \text{ min}^{-1}$ , whereas the A621  $R_p$  and  $S_p$  thio substrates cleaved with rates below the limit of detection (here,  $10^{-4} \text{ min}^{-1}$ ), corresponding to thio effects of at least 3,000-fold. These data suggest that critical catalytic interactions are present at both NPOs. Later, we show that the  $S_p$  thio substrate exhibits metal-ion rescue effects, whereas the  $R_p$  thio substrate does not.

Inspection of the crystal structures shows that the exocyclic amines of G638 and A756 reside spatially close to the scissile phosphate NPOs, and mutational studies<sup>11,14</sup> of these nucleobases have hinted at the importance of their exocyclic amines. To identify potential interactions of the G638 and A756 exocyclic amines with the NPOs, we observed cleavage in ribozymes with the G638 mutated to inosine (G638I), A756 mutated to 3-deazapurine [A756(3cP)] or both (referred to here as 'double mutant') in oxo and stereospecific phosphorothioate backgrounds. The use of 3-deazapurine provides a strategy to test the removal of the exocyclic amine of A without major perturbation to its  $N1$   $pK_a$ .

Both the G638I and A756(3cP) ribozymes exhibit mutational rescues (Table 1) of at least 470 and 390, respectively, suggesting that the exocyclic amines of both G638 and A756 form catalytically important interactions with the pro- $R_p$  NPO of the scissile phosphate (Fig. 1). Interestingly, the double mutant cleaves the  $R_p$  thio substrate with a rate constant of  $0.014 \text{ min}^{-1}$ , corresponding to an inverse thio effect of 6 and a mutational rescue of at least 16,000. The inverse thio effect is unexpected but not without precedent. A similar effect was observed in the *glmS* aporibozyme where, in the absence of cofactor, the 2'-hydroxy at N1 engaged in an unproductive interaction with pro- $R_p$  NPO, which was eliminated in the  $R_p$  thio background<sup>27</sup>. A similar mechanism could explain the inverse thio effect observed here; in the absence of G638:N2 and A756:N6, the pro- $R_p$  NPO might engage the 2'-hydroxy in an unproductive interaction that would prevent the reaction centre from achieving

**Table 1** |  $k_{\text{obs}}$  for cleavage of VS substrates by ribozyme variants under various ionic conditions

Variant	Ionic conditions	Substrate	$k_{\text{obs}}$ ( $\text{min}^{-1}$ )	$k/k'$	$k_o/k_s$	Metal-ion rescue	Mutational rescue
WT	10 mM $\text{Mg}^{2+}$	oxo	$0.32 \pm 0.01$				
		A621 $S_p$	<0.0001		$>3.2 \times 10^3$		
		A621 $R_p$	<0.0001		$>3.2 \times 10^3$		
		A622 $S_p$	$0.0294 \pm 0.0008$		$11 \pm 0.3$		
		A622 $R_p$	<0.0001		$>3.2 \times 10^3$		
	10 mM $\text{Mg}^{2+}$ and	oxo	$0.283 \pm 0.005$				
		A621 $S_p$	$0.0053 \pm 0.0001$		$53 \pm 1.4$	$>60 \pm \text{NA}$	
	20 $\mu\text{M}$ $\text{Cd}^{2+}$	A621 $R_p$	<0.0001		$>2.8 \times 10^3$	NA	
		A622 $S_p$	$0.0328 \pm 0.003$		$8.6 \pm 0.8$	$1.3 \pm 0.1$	
	A622 $R_p$	$0.0190 \pm 0.007$		$15 \pm 5.5$	$>213 \pm \text{NA}$		
G638I	10 mM $\text{Mg}^{2+}$	oxo	$0.0135 \pm 0.0006$	$24 \pm 1.3$			
		A621 $S_p$	<0.0001		$>130$		NA
		A621 $R_p$	$0.0020 \pm 0.0001$		$6.8 \pm 0.5$		$>470 \pm \text{NA}$
	10 mM $\text{Mg}^{2+}$ and	oxo	$0.0141 \pm 0.0005$	$21 \pm 0.8$			
		A621 $S_p$	$0.0009 \pm 0.0001$		$16 \pm 1.8$	$>8.1 \pm \text{NA}$	$3.3 \pm 0.1$
	20 $\mu\text{M}$ $\text{Cd}^{2+}$	A621 $R_p$	$0.0023 \pm 0.0001$		$6.1 \pm 0.3$	$1.1 \pm 0.1$	$>460 \pm \text{NA}$
A756(3cP)	10 mM $\text{Mg}^{2+}$	oxo	$0.0336 \pm 0.0002$	$9.5 \pm 0.3$			
		A621 $S_p$	<0.0001		$>330$		NA
		A621 $R_p$	$0.0041 \pm 0.0001$		$8.2 \pm 0.2$		$>390 \pm \text{NA}$
	10 mM $\text{Mg}^{2+}$ and	oxo	$0.035 \pm 0.002$	$8.1 \pm 0.5$			
		A621 $S_p$	$0.0016 \pm 0.0001$		$22 \pm 1.9$	$>15 \pm \text{NA}$	$2.4 \pm 0.2$
	20 $\mu\text{M}$ $\text{Cd}^{2+}$	A621 $R_p$	$0.0033 \pm 0.0001$		$11 \pm 0.7$	$0.8 \pm 0.1$	$>250 \pm \text{NA}$
G638I	10 mM $\text{Mg}^{2+}$	oxo	$0.0023 \pm 0.0004$	$140 \pm 7.4$			
	and	A621 $S_p$	<0.0001		$>23$		NA
A756(3cP)		A621 $R_p$	$0.0140 \pm 0.0006$		$0.2 \pm 0.1$		$>16 \times 10^3 \pm \text{NA}$
	10 mM $\text{Mg}^{2+}$	oxo	$0.0018 \pm 0.0001$	$160 \pm 9.2$			
	and	A621 $S_p$	$0.0009 \pm 0.0005$		$2 \pm 1.1$	$>12 \pm \text{NA}$	$27 \pm 15$
	20 $\mu\text{M}$ $\text{Cd}^{2+}$	A621 $R_p$	$0.011 \pm 0.003$		$0.2 \pm 0.1$	$1.0 \pm 0.5$	$>14 \times 10^3 \pm \text{NA}$

$k/k'$  corresponds to the ratio  $(k_o^{\text{Mut}}/k_o^{\text{WT}})$ , where the subscript o corresponds to the oxo substrate and the superscripts Mut and WT correspond to a mutant and wild-type ribozyme, respectively.

Metal-ion rescue is calculated according to the ratio of the ratios  $(k_o/k_s)^{\text{Mg}^{2+}}/(k_o/k_s)^{\text{Cd}^{2+}}$ , where the subscript s corresponds to the thio substrate, the superscripts  $\text{Mg}^{2+}$  and  $\text{Cd}^{2+}$  correspond to experiments performed in the presence of  $\text{Mg}^{2+}$  alone and experiments performed in the presence of both  $\text{Mg}^{2+}$  and  $\text{Cd}^{2+}$ , respectively. Mutational rescue corresponds to the ratio of the ratios  $(k_o/k_s)^{\text{WT}}/(k_o/k_s)^{\text{Mut}}$ . The error in the  $k_{\text{obs}}$  measurements is the standard deviation of three or more independent measurements and the errors in the thio effect, metal-ion rescue and mutational rescue are the propagated errors of relative errors. Reactions that proceed slower than the limit of detection (<5% cleavage after 24 h) have been assigned a rate of  $10^{-4} \text{ min}^{-1}$  and cannot be assigned an error ('NA'). Propagated errors as well as ratios based on these measurements are also denoted 'NA'.

an in-line conformation. In the  $R_p$  thio substrate, the sulfur atom would be expected to disrupt this unproductive interaction, resulting in a modest (sixfold) rate enhancement.

To summarize, the loss of reactivity due to a sulfur substitution at the pro- $R_p$  NPO position of the WT ribozyme was recovered to some extent by removing the exocyclic amines of either or both A756 and G638. These observations strongly suggest that the active site is organized by interactions between G638:N2, A756:N6 and the pro- $R_p$  NPO, and the disruption of either or both of these interactions substantially reduces the rate of cleavage.

**Independent MD simulations departing from different crystal structures converge on a functionally inactive state of the ribozyme in the absence of  $\text{Mg}^{2+}$ .** In an effort to unify the VS ribozyme crystal structures with the existing body of solution data, we tested whether molecular motion of the configurations around the scissile phosphate observed in the static crystal structures could plausibly generate active sites consistent with the consensus picture of VS catalysis. We define such active sites as those with in-line

fitness of the nucleophile ( $\tau > 140^\circ$ ) consistent with  $\alpha$  catalysis, and G638 (deprotonated at N1) and A756 (protonated at N1) positioned to act in general base ( $\gamma$ ) and acid ( $\delta$ ) catalysis, respectively, while their exocyclic amines interact with the pro- $R_p$  NPO of the scissile phosphate ( $\beta$  catalysis) as established above. To that end, we carried out MD simulations of the WT ribozyme using all three available crystal structures as departure points so as to ensure that the predictions were independent of the starting state<sup>19,20</sup>. The results of these simulations are summarized in Fig. 2a,b.

Figure 2a depicts the important active-site interactions along the various MD trajectories in the form of interaction maps. These maps report on the probability of observing specific active-site interactions identified from the functional data that support each of the catalytic strategies ( $\alpha$ - $\delta$ ). In the simulations, the putative general base G638 and general acid A756 were kept deprotonated and protonated, respectively, at their N1 positions, assumptions supported by the LFERs described below. According to Fig. 2a, the simulations based on the different crystal structures paint a consistent dynamic picture of the ribozyme active site—one in which each of the key

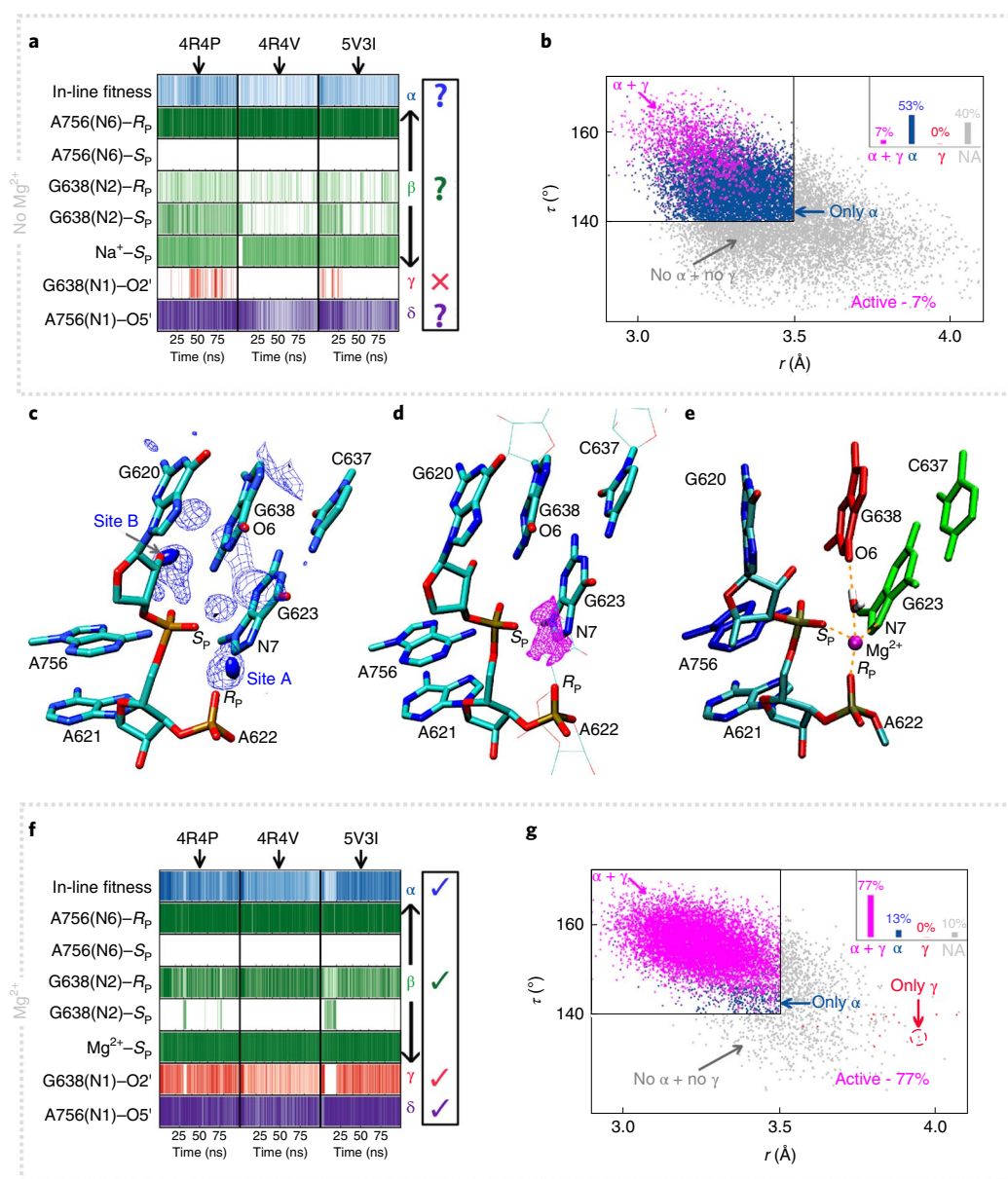


**Fig. 2 | Computational investigation of catalytic strategies adopted by the VS ribozyme.** **a,b**, Summary of the results of MD simulations based on the existing crystal structures. **a**, The persistence of active-site interactions during the various MD simulations. The three columns correspond to simulations departing from the PDB IDs 4R4P, 4R4V and 5V3I crystal structures, and the rows correspond to the interactions related to the different catalytic strategies ( $\alpha$ – $\delta$ ). The first row refers to in-line fitness, which is dictated by the  $\tau$ (O2'–P–O5') angle ( $\geq 140^\circ$ ) and the O2'–P distance ( $\leq 3.5$  Å). Hydrogen-bonding and metal-ion interaction distance thresholds ( $\beta$ – $\delta$ ) were chosen to be  $\leq 2$  and  $\leq 2.5$  Å, respectively. The rightmost rectangle summarizes the interaction plot. **b**, The 2D scatter plot of the in-line attack angle  $\tau$  and O2'–P distance ( $r$ ) and includes data from all MD simulations. The data points are classified into four categories: configurations that exhibit both  $\alpha$  and  $\gamma$  catalysis (magenta), only  $\alpha$  catalysis (blue), only  $\gamma$  catalysis (red) and configurations that do not exhibit either  $\alpha$  or  $\gamma$  catalysis (NA, non-active, grey). Data points corresponding to the different categories are indicated by arrows and the black box outlines the region that exhibits  $\alpha$  catalysis. **c**, Illustration of the  $\text{Na}^+$  charge isodensity plots in the active-site region calculated from MD simulations. To construct these isodensity plots, a 3D cubic grid having an edge length of 12 Å and spacing of 1 Å was centred on the phosphorus atom of the scissile phosphate. For a given MD trajectory, the total charge per grid cell was determined by summing over the charges of all ions in that particular cell. The blue solid surface and the mesh represent the top 30 and 70% of the charge density of the entire grid, respectively. **d**, Illustration of the  $\text{Mg}^{2+}$  binding site predicted by 3D-RISM calculations. The magenta surface represents the top 10% of  $\text{Mg}^{2+}$  isodensity. **e**, Depiction of the  $\text{Mg}^{2+}$ -bound active-site model obtained from MD simulations. In this model,  $\text{Mg}^{2+}$  forms inner-sphere contacts with the A621 pro- $S_P$  NPO, A622 pro- $R_P$  NPO and G623:N7, and interacts with G638:O6 through a water molecule. **f,g**, Summary of the results of the MD simulations based on the crystal structures but with an added  $\text{Mg}^{2+}$  bound at the pro- $S_P$  NPO of the scissile phosphate. Panels **f** and **g** are analogous to panels **a** and **b**, respectively.

elements of catalysis ( $\alpha$ ,  $\beta$ ,  $\gamma$ , and  $\delta$ ) is either absent or not present in full strength to support efficient catalysis and hence does not reflect an active state in solution. Most concerning in the simulations was the lack of formation of a catalytically active state characterized by

in-line fitness and positioning of the O2' nucleophile for activation ( $\alpha$  and  $\gamma$  catalysis, respectively), which accounted for only a small fraction (7%) of all the configurations (Fig. 2b). Taken together, the results of these MD simulations suggest that the active-site ensemble

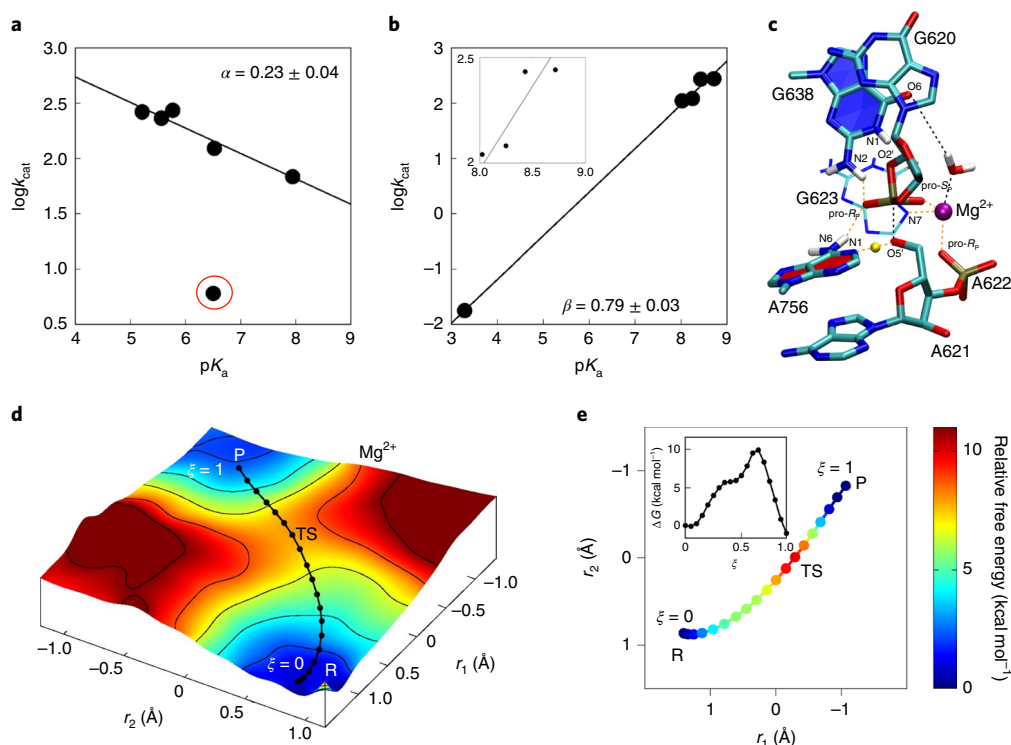


**Fig. 3 | Catalytic mechanism of the VS ribozyme.** **a**, Brønsted plot for VS ribozymes with A756 analogues. The  $k_{\text{cat}}$  and  $pK_{\text{a}}$  values were determined by fitting pH profiles (Supplementary Fig. 6) to a model for double ionization. For all the A analogues, the lower  $pK_{\text{a}}$  was assumed to correspond to the general acid (A756 in WT ribozyme). The data (excluding the outlier 3Cp mutant circled in red) were fit linearly to reveal a slope of  $0.23 \pm 0.04$ . **b**, Brønsted plot for VS ribozymes with G638 analogues. The  $k_{\text{cat}}$  and  $pK_{\text{a}}$  values were determined by fitting pH profiles (Supplementary Fig. 7) to a model for double ionization with the exception of the G638P\* substrate, which was fit to a model for single ionization. For all the G analogues, the higher  $pK_{\text{a}}$  was assumed to correspond to the general base (G638 in WT ribozyme). The  $pK_{\text{a}}$  of P\* (3.3) was inferred from titration of the nucleoside in solution. The linear fitting of the resulting plot revealed a slope of  $0.79 \pm 0.03$ . The inset expands the data points that fall in the  $pK_{\text{a}}$  range 8–9. The linear fitting of only these data points and excluding the data point corresponding to P\* ( $pK_{\text{a}} = 3.3$ ) results in a slope of  $0.67 \pm 0.04$ . **c**, The 3D structure of a representative transition-state geometry along the reaction pathway obtained in the presence of active-site  $\text{Mg}^{2+}$ . **d**, The 2D free-energy surface underlying the catalytic reaction obtained using ab initio QM/MM US simulations. The solid black line corresponds to the converged pathway obtained using FTS simulations. **e**, Converged pathway obtained from the FTS simulations in the presence of active-site  $\text{Mg}^{2+}$ . In **d** and **e**, the reaction coordinate  $r_1$  corresponds to the phosphorus bond breaking/forming coordinate represented by the difference between the A621:P–G620:O2' and A621:P–A621:O5' distances, and  $r_2$  corresponds to the general acid proton transfer coordinate represented by the difference between the A756:N1–A756:H1 and A621:O5'–A756:H1 distances. The colour scale denotes relative free-energy values in units of  $\text{kcal mol}^{-1}$ . R, reactant; TS, transition state; P, product;  $\xi$ , reduced length of the curve (unitless).

emerging from simulations based on the existing ribozyme crystal structures, does not reflect the catalytically active state of the ribozyme in solution under standard conditions. A detailed discussion of Fig. 2a,b is provided in the Supplementary Information.

**MD simulations and molecular solvation theory calculations predict a  $\text{Mg}^{2+}$  binding site at the active site.** No divalent metal ions were observed at the active site in the VS ribozyme crystal structures, possibly because they were obtained in the presence of high ammonium ion concentrations. However, spectroscopic data<sup>28–32</sup> suggest that VS activity depends on multiple localized divalent ions. VS cleavage typically requires  $\text{Mg}^{2+}$  ions for activity, except in very high concentrations of monovalent ions<sup>33</sup>. The ribozyme is not active in cobalt hexamine alone, but in the presence of small amounts of  $\text{Mg}^{2+}$ , cobalt hexamine enhances catalysis<sup>34</sup>. The  $\text{Mg}^{2+}$  concentration dependence of ribozyme folding, inferred from hydroxyl radical footprinting, was estimated to be an order of magnitude lower than that required for catalysis<sup>35</sup>. Taken together, these studies indicate that  $\text{Mg}^{2+}$  ions are not only important for global folding, but are more directly involved in interactions (either in organization or transition-state stabilization) at the active site that affect catalysis.

Analysis of the MD trajectories revealed two sites in the active site where  $\text{Na}^+$  ions bind with high occupancy (Fig. 2c). Site A is at the pro- $S_{\text{p}}$  NPO of the scissile phosphate, and site B is between the 2' O nucleophile and the pro- $R_{\text{p}}$  NPO of the scissile phosphate. To identify probable  $\text{Mg}^{2+}$  binding sites, we carried out three-dimensional reference interaction site model (3D-RISM) calculations<sup>36,37</sup> on the different crystal structures as well as on the configurations obtained from the simulations. The results of the 3D-RISM calculations predict a high probability of  $\text{Mg}^{2+}$  binding at site A in the active site (Fig. 2d). A  $\text{Mg}^{2+}$  at this position is consistent with the previously reported thio effects<sup>25</sup> observed for a mixture of diastereoisomers of the scissile phosphate (although this was not rescued in the presence of  $\text{Mn}^{2+}$ ) and at the phosphate of the N+1 nucleotide (A622) downstream of the scissile phosphate. Thus, the analysis of  $\text{Na}^+$  binding at the active site and the results of 3D-RISM calculations jointly suggest that site A, the position coordinating the pro- $S_{\text{p}}$  NPO of A621 (the scissile phosphate) and close to the pro- $R_{\text{p}}$  NPO of A622 and the N7 of G623, is a plausible  $\text{Mg}^{2+}$  binding site.

**Metal-ion rescue experiments confirm  $\text{Mg}^{2+}$  is bound stereospecifically at the pro- $S_{\text{p}}$  non-bridging position.** Given the large thio effects observed and the computational prediction that a divalent

metal ion likely occupies a position near the active site, we tested the rate of cleavage of the A621  $R_p$  and  $S_p$  thio substrates in the presence of a thiophilic metal ion. Metal-ion rescue for the scissile phosphate has been investigated in two previous studies and no rescue was observed. However, as mentioned previously, those studies were complicated by the use of a mixture of diastereomeric substrates<sup>25</sup> or the observation of the reverse reaction rather than cleavage<sup>26</sup>. Furthermore, both studies tested for rescue in the presence of  $Mn^{2+}$  rather than the more thiophilic  $Cd^{2+}$ . We investigated metal-ion rescue with  $Cd^{2+}$  in a background of 10 mM  $Mg^{2+}$  in an effort to identify the putative metal ion binding site. The results are summarized in Table 1. In the oxo background,  $Cd^{2+}$  has a minimal impact on the rate of cleavage at low concentration, but inhibits cleavage when the concentration of  $Cd^{2+}$  approaches the concentration of  $Mg^{2+}$ . The presence of 20  $\mu M$   $Cd^{2+}$  increased the rate constant of cleavage for the  $S_p$  thio substrate to 0.0053  $min^{-1}$ , corresponding to at least a 53-fold enhancement over the rate of cleavage in the absence of  $Cd^{2+}$  and a metal-ion rescue of at least 60. Note, the actual metal-ion rescue is somewhat higher, but because the actual rate in the absence of  $Cd^{2+}$  is less than the limit of detection, we assume a rate of  $10^{-4} min^{-1}$ . In contrast to the  $S_p$  thio substrate, the  $R_p$  thio substrate exhibits no enhanced cleavage in the presence of  $Cd^{2+}$ , corresponding to no metal-ion rescue, indicating that the stimulatory effect of the thiophilic metal is site specific. Additionally, we tested the effect of metal-ion rescue in the G638I, A756(3cP) and double-mutant ribozyme backgrounds and observed metal-ion rescues of at least 8, 15 and 12, respectively, for the  $S_p$  thio substrate and no metal-ion rescue for the  $R_p$  thio substrate for each variant. These data provide support for a mechanism in which a divalent metal ion specifically coordinates to the pro- $S_p$  NPO in the ribozyme active site.

**Simulations with an active-site  $Mg^{2+}$  converge on a functionally active state of the ribozyme.** Motivated by the results from the metal-ion rescue experiments, we sought to investigate the ramifications of a  $Mg^{2+}$  ion for the ribozyme active site dynamics. We re-propagated the MD trajectories, departing from each of the different crystal structures and having G638 and A756 in their active protonation states as previously, but with a  $Mg^{2+}$  bound at the A621 pro- $S_p$  NPO as well as close to the pro- $R_p$  NPO of A622 and the N7 of G623 as predicted above (site A in the active site, Fig. 2c–e). The results of these simulations are summarized in Fig. 2f,g. Interestingly, as illustrated by the interaction maps (Fig. 2f), these independent trajectories converge to an active-site ensemble that agrees with the experimental data and exhibits all the key catalytic strategies.

For the simulations in the presence of a  $Mg^{2+}$  bound at site A in the active site, the majority of the configurations (77%) sampled showed a catalytically active state (exhibiting both  $\alpha$  and  $\gamma$  catalysis), compared with only 7% of the configurations in the simulations without  $Mg^{2+}$ . This 11-fold increase in active configurations observed in the MD simulations in the presence of  $Mg^{2+}$  at site A suggests that the metal ion enhances catalysis, at least in part, by organizing the active site.

The  $Mg^{2+}$ -bound model of the active site emerging from these MD simulations is shown in Fig. 2e and Supplementary Fig. 3. The  $Mg^{2+}$  remains mostly localized in the simulations, and apart from the scissile phosphate A621 pro- $S_p$  NPO, maintains an inner-sphere contact with the N7 of G623. In two of the three simulations, the metal ion also maintains an inner-sphere contact with the A622 pro- $R_p$  NPO and interacts with G638:O6 through a water molecule, whereas in the third simulation, the metal ion moves in the active site to form an inner-sphere contact with G638:O6 and interacts with the A622 pro- $R_p$  NPO through a water molecule. In each of the simulations, two other water molecules complete the hexacoordination of the ion.

**Mutation experiments further validate the  $Mg^{2+}$ -bound model.** We sought to validate the  $Mg$ -bound model (Fig. 2e), first, by

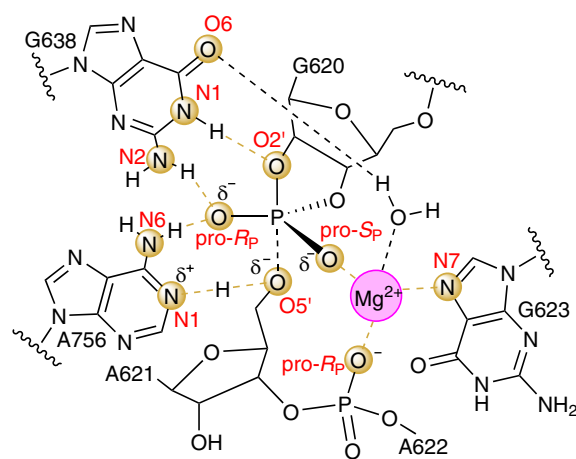


**Fig. 4 | An elaborate network of interactions configures the VS ribozyme for proton transfer and transition-state stabilization.** The 2D schematic of the transition-state configuration developed in this work. The transition state is a ‘late’ transition state in which the P–O2’ bond is almost fully formed, the P–O5’ bond is mostly broken and the proton from A756 is partly transferred to the 5’O leaving group, consistent with the LFER data and suggesting that the proton transfer from G638 probably occurs in a pre-equilibrium step before arriving at the rate-controlling transition state. Atoms and dashed-line connections highlighted in gold indicate the functional linkages established in this study. Dashed-line connections indicate the forming and breaking O–P bonds and the H atom in flight from A756 to O5’.

testing for metal-ion rescue at the downstream phosphate, A622. Previous studies showed a substantial thio effect at the phosphorothioate downstream of the scissile phosphate rescuable with  $Mn^{2+}$  (refs. 25,38), but there was a lack clarity in the stereochemistry of the putative metal–phosphate interaction. In the presence of 10 mM  $Mg^{2+}$ , the A622: $S_p$  thio substrate cleaves with a rate constant of 0.029  $min^{-1}$ , corresponding to a modest thio effect of about 11. The A622: $R_p$  thio substrate, on the other hand, cleaves with a rate below the limit of detection, corresponding to a thio effect of at least 3,000. In the presence of 20  $\mu M$   $Cd^{2+}$ , cleavage of the A622: $S_p$  thio substrate is virtually unaffected, but cleavage of the A622: $R_p$  thio substrate is accelerated at least 190-fold, having a rate constant of 0.019  $min^{-1}$ , corresponding to a metal rescue of at least 213. These data strongly suggest that the pro- $R_p$  NPO of the phosphate downstream of the cleavage centre coordinates a divalent metal ion, consistent with the computational prediction. We also tested cleavage with a G623(7cG) ribozyme variant, which eliminates the putative G623:N7– $Mg^{2+}$  interaction. This ribozyme failed to cleave the phosphate substrate at a detectable rate, implying that G623:N7 plays an important role in catalysis. Regarding the predicted outer-sphere  $Mg^{2+}$  interaction with G638:O6, the unique configuration of 7-deaza-5-azaguanosine (a member of the hachimoji alphabet<sup>5,39–41</sup> and referred to herein as P\*) enables a strategy to test for a possible role of the O6 keto group. P\* deprotonates with the same  $pK_a$  as 2-aminopurine riboside (2-amP) and differs from 2-aminopurine on the Watson–Crick face only by the presence of the keto group (Supplementary Fig. 5). In contexts where N7 makes no interactions (as in G638 of the VS ribozyme), comparisons of RNAs bearing P\* versus 2-amP can reveal the functional significance of the O6 keto group of a G residue. At all pH values tested, a substrate containing the G638P\* mutation reacts significantly faster than a substrate containing G638(2amP), consistent with an interaction involving the O6 keto group.

In summary, the phosphorothioate and subsequent metal-ion rescue effect observed at the A622 pro- $R_p$  NPO, the inactivity of the

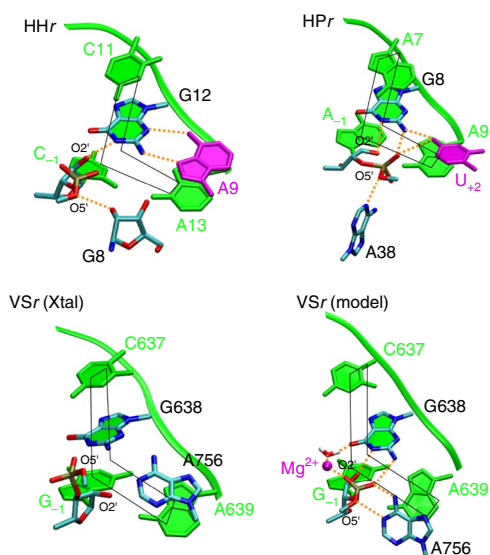


**Fig. 5 | The hammerhead (HHr), hairpin (HPr) and VS(VSr) ribozymes use distinct strategies to anchor the L-platform.** The active sites in the crystal structures of the three ribozymes are compared with the Mg<sup>2+</sup>-bound VS ribozyme model (VSr (model)) proposed in this work to highlight common features. In this figure, the hairpin, hammerhead and VS ribozyme active sites are based on PDB IDs 1M5O<sup>52</sup>, 3ZP8<sup>51</sup> and 5V3I<sup>20</sup>, respectively. Each of the ribozyme active sites exhibit the L-platform motif (the L-shape is indicated by black lines) formed by the N-1 nucleotide, the residue immediately preceding the scissile phosphate, and nucleotide 3' to the general base as the short arm of the L and the N-1 nucleotide, the general base itself and the nucleotide 5' to the general base as the long arm of the L. Both the hammerhead and hairpin contain an L-anchor residue (shown in purple)<sup>53</sup> that engages with the general base and presumably holds it in position; this active-site feature is lacking in the VS ribozyme crystal structures. The Mg<sup>2+</sup>-bound model defined in this study suggests that the metal ion steps into the role of the L-anchor, interacting with G638 and positioning the base for catalysis.

G623(7cG) ribozyme variant and greater reactivity of the G638P\* variant compared with G638(2amP) (the latter does not have the O6 keto group) suggest that Mg<sup>2+</sup> interacts with the A622 pro-R<sub>p</sub> NPO, G623:N7 and G638:O6 (through a coordinated water molecule), respectively, and provide crucial evidence in support of our proposed metal binding site.

**LFERs suggest proton transfer is nearly complete for the general base and partial for the general acid in the transition state.** The consensus view of VS catalysis holds that G638 and A756 function as general base and general acid, respectively<sup>22,42</sup>. Although evidence exists to support these hypotheses<sup>11,14–18</sup>, significant gaps in our understanding remain. For instance, phosphorothiolate rescue experiments<sup>17</sup> demonstrated a functional linkage between A756 and the 5' O leaving group, but those data leave open the possibility of catalysis through some mechanism other than proton transfer to the leaving group. Also, although pH–rate profiles implicate the titration of G638, no data to-date establish a functional linkage between G638 and the 2' O nucleophile. Moreover, nothing is known about the nature of the transition state in terms of the extent of proton transfer from the general acid and to the general base. To shed light on these aspects of VS ribozyme catalysis, we measured Brønsted coefficients for a series of ribozymes with A and G analogues (see Supplementary Information for details).

To test the extent of proton transfer between the general acid, A756, and the 5' O leaving group, we measured the rate of

cleavage over a range of pH values for ribozymes with adenosine (WT), 3-deazaadenosine (3cA), 7-deazaadenosine (7cA), 8-azaadenosine (8nA), 8-aza-7-deazaadenosine (8n7cA) or 3-deazapurine (3cP) at the 756 position. The observed linear relationship observed in the Brønsted plot for these A analogues, excluding 3cP (Fig. 3a), strongly suggests that A756 is involved in proton transfer and the expected deviation from linearity observed for the A756(3cP) ribozyme results from the elimination of A756:N6, which coordinates the pro-R<sub>p</sub> NPO of the scissile phosphate. The small Brønsted coefficient observed ( $\alpha = 0.23 \pm 0.04$ ) indicates that (1) proton transfer from A756 occurs in the rate-controlling step and not in a pre-equilibrium step and (2) the extent of proton transfer is only partial in the transition state. In contrast, proton transfer to the leaving group in the hepatitis delta virus ribozyme appears to be significantly more advanced<sup>43</sup>.

We repeated the same procedure to investigate proton transfer to the putative general base, G638, with a series of substrates containing guanosine (WT), 7-deazaguanosine (7cG), 8-azaguanosine (8nG), 6-thioguanosine (6sG) or 7-deaza-5-azaguanosine (P\*) at the 638 position. The Brønsted plot constructed for the G analogues reveal a linear dependence on pK<sub>a</sub> of the G analogues with a slope close to 1 ( $\beta = 0.79 \pm 0.03$ ; Fig. 3b). Considering the uncertainty of the data point at pK<sub>a</sub> = 3.3, due to the need to estimate the reaction pK<sub>a</sub> from the nucleobase solution pK<sub>a</sub>, the derived  $\beta$  slope of 0.79 should be viewed with caution and considered a rough estimate for the degree of proton transfer to the nucleobase. Omission of the data point at pK<sub>a</sub> = 3.3, which limits the data set to a relatively narrow pK<sub>a</sub> range (8–9), yields a modestly attenuated slope ( $\beta$  value) of  $0.67 \pm 0.04$ . Despite these limits to their quantitative interpretation, the data qualitatively support a mechanism involving substantial proton transfer from the nucleophile to the general base in the transition state.

Taken together, the LFER data strongly support the roles of the catalytic nucleobases A756 and G638 in general acid–base catalysis established previously by Lilley and co-workers<sup>11,12,14,15,17,22</sup> and provide additional information about the nature of the transition state involving each of the proton transfer steps. Proton transfer between A756 and the 5' O leaving group occurs in the rate-controlling step and the extent of transfer is partial in the transition state. Brønsted analysis also implicates G638 in proton transfer. The data suggest that proton transfer from the nucleophile has advanced significantly in the transition state but lack the resolution to distinguish between pre-equilibrium or concerted proton transfer for the catalytic guanine. The computational results presented below provide predictive insight to resolve this ambiguity.

**QM/MM free-energy simulations departing from the Mg<sup>2+</sup>-bound model predict a catalytic mechanism that is consistent with the LFER data.** We calculated the free-energy surface and the minimum free-energy pathway associated with the catalytic reaction by combining semi-empirical finite temperature string (FTS) simulations<sup>44,45</sup> and ab initio 1D and 2D QM/MM umbrella sampling (US) simulations (details are provided in the Supplementary Information). The FTS simulations suggested a sequential catalytic pathway in which the 2' O nucleophile deprotonation by G638 occurs initially, as a separate step, followed by concerted nucleophilic attack and departure of the leaving group; the associated free-energy profile along the pathway suggested the latter to be rate-limiting (Supplementary Fig. 9). This result is consistent with the Brønsted analysis of the G638 analogues, and together they support a mechanism in which the proton transfer from the 2' O hydroxy nucleophile occurs in a pre-equilibrium step.

The chemical step of the reaction was studied in more detail using ab initio 2D QM/MM US simulations. The 2D free-energy surface calculated from these ab initio simulations (Fig. 3d) is in excellent agreement with the converged pathway obtained from

the semi-empirical FTS simulations (see Supplementary Fig. 10 for direct comparison) and suggests that the P–O2'/P–O5' bond formation/cleavage and general acid proton transfer to the leaving group occur in a concerted fashion. To obtain a better resolution of the free energy along the reaction pathway, we performed additional *ab initio* 1D US along the converged pathway obtained from the FTS simulations, the results of which are shown in Fig. 3d,e. The free-energy barrier of the reaction obtained from these simulations is  $\sim 10$  kcal mol<sup>-1</sup>, which, using the Arrhenius rate model, corresponds to an intrinsic rate constant of  $\sim 10^4$  s<sup>-1</sup> (assuming a pre-factor of 1 ps<sup>-1</sup>). This calculated rate constant is consistent with the intrinsic rates obtained for certain fast-cleaving VS constructs ( $1.4 \times 10^3$  s<sup>-1</sup>)<sup>18,46</sup>, but is somewhat higher than the rates observed in this work. Presumably, fast dynamic equilibria reduce the observed rate of cleavage, especially in the *trans* constructs employed in this study that require substrate docking; these processes are not accounted for in the QM/MM calculations. Thus, the estimated rate constant obtained from the simulations represents an upper limit of plausible intrinsic rate constants. The transition state obtained from these simulations (Fig. 3c) is a 'late' transition state, in which the P–O2' bond is almost fully formed, the P–O5' bond is mostly broken and the proton from A756 is partly transferred to the 5' O leaving group, consistent with the LFER data and further suggesting that the proton transfer from G638 likely occurs in a pre-equilibrium step prior to arriving at the rate-controlling transition state.

To summarize, the QM/MM simulations departing from the Mg<sup>2+</sup>-bound model suggest a mechanism in which the 2' O nucleophile activation by the general base occurs in a pre-equilibrium proton transfer step; the rate-controlling step consists of the P–O2'/P–O5' bond formation/cleavage and general acid proton transfer to the 5' O leaving group. The free-energy barrier for this step is consistent with the ribozyme intrinsic reaction rates and passes through a 'late' transition state in which the P–O2' bond is mostly formed, the P–O5' bond is mostly broken and the proton from the general acid has partially transferred to the 5' O leaving group, in agreement with the LFER data.

## Discussion

Ribozymes use two main chemical moieties for catalysis: metal ions and nucleobases. From biophysical studies spanning nearly three decades, the consensus view held that the VS catalytic mechanism depended entirely on nucleobase catalysis and the contributions of metal ions were restricted to structural organization<sup>12,22</sup>. Herein, we have presented a combination of computational and experimental data that converge on a configuration of interactions within the active site that imparts catalysis (Fig. 4), including a newly identified divalent metal ion that interacts with the pro-S<sub>p</sub> oxygen of the scissile phosphate and helps to organize the active site through additional inner-sphere coordination to the pro-R<sub>p</sub> oxygen of the downstream phosphate (A622) and G623:N7 as well as an outer-sphere coordination to G638:O6.

Before this work, it was speculated that the VS and hairpin ribozymes were mechanistically nearly identical, having topologically similar active sites and employing exclusively nucleobase catalysis in their cleavage mechanisms<sup>12</sup>. In our previous study<sup>19</sup>, based on the then-recent VS structural data, we took the parallels in these ribozymes a step further by illustrating that both VS and hairpin ribozymes, along with the hammerhead ribozyme, share a common active-site scaffold, referred to as the L-platform, an L-shaped motif in which the N-1 nucleotide, the residue immediately preceding the scissile phosphate, makes the corner of the L, the nucleotide 3' to the general base forms the short arm of the L and the nucleotide 5' to the general base forms the long arm of the L along with the general base (Fig. 5). The presence of this L-shaped motif in three distinct ribozyme classes implicates the L-platform motif as a

functional strategy to position the N-1 nucleotide and direct the general base towards the 2'-hydroxy group.

Our joint experimental and computational efforts illustrate that despite having the L-platform, the VS ribozyme fails to exhibit the key catalytic interactions in the absence of the active-site Mg<sup>2+</sup>, implying that the presence of the L-platform alone may not be sufficient to position the general base. Considering this new data, we went back to the hairpin and hammerhead crystal structures, as well as the subsequently determined twister ribozyme structure, and found that these ribozymes have an active-site nucleotide, referred to here as the L-anchor, that interacts with the general base and presumably contributes to its positioning for nucleophile activation. In hammerhead ribozymes, a conserved adenine (A21) serves as the L-anchor, whereas in hairpin ribozymes an invariant uracil (U+2) serves this role. In the currently available structural data, the VS ribozyme lacks a nucleobase that could plausibly serve the role of the L-anchor. However, inspection of the model of the VS ribozyme defined in this work suggests that the newly identified Mg<sup>2+</sup> may serve as the L-anchor, fulfilling the role served by a nucleobase in the hairpin and hammerhead ribozymes. The metal ion assists in organizing the active site through direct stereospecific interactions with the A621 and A622 phosphates and G623:N7 as well as a water-mediated interaction with G638:O6. The outer-sphere interaction between the Mg<sup>2+</sup> and G638:O6, supported functionally by the higher reaction rates of the G638P mutant as compared with the G638(2amP) mutant, may also assist in shifting the G638 pK<sub>a</sub> to its apparent value of 8.4. Similar pK<sub>a</sub> tuning of the general base caused by divalent metal ion binding has been observed in X-ray structures<sup>47,48</sup> of the hammerhead ribozyme at elevated pH and have been subsequently interpreted mechanistically in recent computational work<sup>49</sup>.

Thus, although our studies corroborate the existing notion that the VS ribozyme bears mechanistic similarity to the hairpin ribozyme<sup>12</sup>, they reveal previously unknown facets of the VS ribozyme active-site architecture and elicit mechanistic similarities to the hammerhead ribozyme. In one view, VS is hairpin-like in that it utilizes the same nucleobase residues to carry out general acid–base catalysis. However, the two ribozymes differ in terms of how the catalytic nucleobases utilize their exocyclic amines and by the presence of an active-site Mg<sup>2+</sup> that the VS requires for catalysis. The role of Mg<sup>2+</sup> in VS is both organizational, as an anchoring construct, and electrostatic, in tuning the pK<sub>a</sub> of the general base and presumably in stabilizing the transition state through interaction with the scissile phosphate. Like the VS ribozyme, the hammerhead ribozyme uses a guanine as general base and requires a conserved adenine and Mg<sup>2+</sup> for catalysis. However, the roles of the adenine and Mg<sup>2+</sup> are reversed in the two ribozymes: in VS A756 provides general acid catalysis and Mg<sup>2+</sup> serves as the L-anchor<sup>50</sup>, whereas in hammerhead the Mg<sup>2+</sup> assists in acid catalysis<sup>51</sup> and A9 serves as the L-anchor<sup>50</sup>. Taken together, these observations reveal new functional features shared by the hammerhead, hairpin and VS ribozymes.

## Online content

Any Nature Research reporting summaries, source data, extended data, supplementary information, acknowledgements, peer review information; details of author contributions and competing interests; and statements of data and code availability are available at <https://doi.org/10.1038/s41557-019-0391-x>.

Received: 12 March 2019; Accepted: 13 November 2019;  
Published online: 20 January 2020

## References

1. Abelson, J. The discovery of catalytic RNA. *Nat. Rev. Mol. Cell. Biol.* **18**, 653 (2017).
2. Symons, R. H. Small catalytic RNAs. *Ann. Rev. Biochem.* **61**, 641–671 (1992).

3. Herschlag, D. & Cech, T. R. Catalysis of RNA cleavage by the Tetrahymena thermophila ribozyme. I. Kinetic description of the reaction of an RNA substrate complementary to the active site. *Biochemistry* **29**, 10159–10171 (1990).
4. Narlikar, G. J. & Herschlag, D. Mechanistic aspects of enzymatic catalysis: lessons from comparison of RNA and protein enzymes. *Ann. Rev. Biochem.* **66**, 19–59 (1997).
5. Hoshika, S. et al. Hachimioji DNA and RNA: a genetic system with eight building blocks. *Science* **363**, 884–887 (2019).
6. Jimenez, R. M., Polanco, J. A. & Lupták, A. Chemistry and biology of self-cleaving ribozymes. *Trends Biochem. Sci.* **40**, 648–661 (2015).
7. Wilson, T. J., Liu, Y. & Lilley, D. M. J. Ribozymes and the mechanisms that underlie RNA catalysis. *Front. Chem. Sci. Eng.* **10**, 178–185 (2016).
8. Kennell, J. C. et al. The VS catalytic RNA replicates by reverse transcription as a satellite of a retroplasmid. *Gene Dev.* **9**, 294–303 (1995).
9. Saville, B. J. & Collins, R. A. A site-specific self-cleavage reaction performed by a novel RNA in neurospora mitochondria. *Cell* **61**, 685–696 (1990).
10. Lafontaine, D. A., Norman, D. G. & Lilley, D. M. J. The global structure of the VS ribozyme. *EMBO J.* **21**, 2461–2471 (2002).
11. Lafontaine, D. A., Wilson, T. J., Zhao, Z. Y. & Lilley, D. M. J. Functional group requirements in the probable active site of the VS ribozyme. *J. Mol. Biol.* **323**, 23–34 (2002).
12. Wilson, T. J. & Lilley, D. M. J. Do the hairpin and VS ribozymes share a common catalytic mechanism based on general acid-base catalysis? A critical assessment of available experimental data. *RNA* **17**, 213–221 (2011).
13. Hiley, S. L., Sood, V. D., Fan, J. & Collins, R. A. 4-thio-U cross-linking identifies the active site of the VS ribozyme. *EMBO J.* **21**, 4691–4698 (2002).
14. Wilson, T. J., McLeod, A. C. & Lilley, D. M. J. A guanine nucleobase important for catalysis by the VS ribozyme. *EMBO J.* **26**, 2489–2500 (2007).
15. Lafontaine, D. A., Wilson, T. J., Norman, D. G. & Lilley, D. M. J. The A730 loop is an important component of the active site of the VS ribozyme. *J. Mol. Biol.* **312**, 663–674 (2001).
16. Jaikaran, D., Smith, M. D., Mehdizadeh, R., Olive, J. & Collins, R. A. An important role of G638 in the *cis*-cleavage reaction of the *Neurospora* VS ribozyme revealed by a novel nucleotide analog incorporation method. *RNA* **14**, 938–949 (2008).
17. Wilson, T. J. et al. Nucleobase-mediated general acid-base catalysis in the Varkud satellite ribozyme. *Proc. Natl Acad. Sci. USA* **107**, 11751–11756 (2010).
18. Smith, M. D. & Collins, R. A. Evidence for proton transfer in the rate-limiting step of a fast-cleaving Varkud satellite ribozyme. *Proc. Natl Acad. Sci. USA* **104**, 5818–5823 (2007).
19. Suslov, N. B. et al. Crystal structure of the Varkud satellite ribozyme. *Nat. Chem. Biol.* **11**, 840–846 (2015).
20. DasGupta, S., Suslov, N. B. & Piccirilli, J. A. Structural basis for substrate helix remodeling and cleavage loop activation in the Varkud satellite ribozyme. *J. Am. Chem. Soc.* **139**, 9591–9597 (2017).
21. Collins, R. A. The *Neurospora* Varkud satellite ribozyme. *Biochem. Soc. Trans.* **30**, 1122–1126 (2002).
22. Lilley, D. M. J. The Varkud satellite ribozyme. *RNA* **10**, 151–158 (2004).
23. Bevilacqua, P. C. et al. An ontology for facilitating discussion of catalytic strategies of RNA-cleaving enzymes. *ACS Chem. Biol.* **14**, 1068–1076 (2019).
24. Emilsson, G. M., Nakamura, S., Roth, A. & Breaker, R. R. Ribozyme speed limits. *RNA* **9**, 907–918 (2003).
25. Kovacheva, Y. S., Tzokov, S. B., Murray, I. A. & Grasby, J. A. The role of phosphate groups in the VS ribozyme–substrate interaction. *Nucleic Acids Res.* **32**, 6240–6250 (2004).
26. Zamel, R. & Collins, R. A. Rearrangement of substrate secondary structure facilitates binding to the *Neurospora* VS ribozyme. *J. Mol. Biol.* **324**, 903–915 (2002).
27. Bingaman, J. L. et al. The GlcN6P cofactor plays multiple catalytic roles in the *glmS* ribozyme. *Nat. Chem. Biol.* **13**, 439–445 (2017).
28. Campbell, D. O. & Legault, P. Nuclear magnetic resonance structure of the Varkud satellite ribozyme stem-loop V RNA and magnesium-ion binding from chemical-shift mapping. *Biochemistry* **44**, 4157–4170 (2005).
29. Campbell, D. O., Bouchard, P., Desjardins, G. & Legault, P. NMR structure of Varkud satellite ribozyme stem-loop V in the presence of magnesium ions and localization of metal-binding sites. *Biochemistry* **45**, 10591–10605 (2006).
30. Bonneau, E. & Legault, P. Nuclear magnetic resonance structure of the III–IV–V three-way junction from the Varkud satellite ribozyme and identification of magnesium-binding sites using paramagnetic relaxation enhancement. *Biochemistry* **53**, 6264–6275 (2014).
31. Bonneau, E. & Legault, P. NMR localization of divalent cations at the active site of the *Neurospora* VS ribozyme provides insights into RNA–metal-ion interactions. *Biochemistry* **53**, 579–590 (2014).
32. Dagenais, P., Girard, N., Bonneau, E. & Legault, P. Insights into RNA structure and dynamics from recent NMR and X-ray studies of the *Neurospora* Varkud satellite ribozyme. *WIREs RNA* **8**, e1421 (2017).
33. Murray, J. B., Seyhan, A. A., Walter, N. G., Burke, J. M. & Scott, W. G. The hammerhead, hairpin and VS ribozymes are catalytically proficient in monovalent cations alone. *Chem. Biol.* **5**, 587–595 (1998).
34. Maguire, J. L. & Collins, R. A. Effects of cobalt hexammine on folding and self-cleavage of the *Neurospora* VS ribozyme. *J. Mol. Biol.* **309**, 45–56 (2001).
35. Tzokov, S. B., Murray, I. A. & Grasby, J. A. The role of magnesium ions and 2′-hydroxyl groups in the VS ribozyme–substrate interaction. *J. Mol. Biol.* **324**, 215–226 (2002).
36. Luchko, T. et al. Three-dimensional molecular theory of solvation coupled with molecular dynamics in Amber. *J. Chem. Theory Comput.* **6**, 607–624 (2010).
37. Genheden, S., Luchko, T., Gusarov, S., Kovalenko, A. & Ryde, U. An MM/3D-RISM approach for ligand binding affinities. *J. Phys. Chem. B* **114**, 8505–8516 (2010).
38. Sood, V. D., Beattie, T. L. & Collins, R. A. Identification of phosphate groups involved in metal binding and tertiary interactions in the core of the *Neurospora* VS ribozyme. *J. Mol. Biol.* **282**, 741–750 (1998).
39. Kim, S. H., Bartholomew, D. G., Allen, L. B., Robins, R. K. & Revankar, G. R. Imidazo[1,2-*a*]-*s*-triazine nucleosides. Synthesis and antiviral activity of the N-bridgehead guanine, guanosine, and guanosine monophosphate analogues of imidazo[1,2-*a*]-*s*-triazine. *J. Med. Chem.* **21**, 883–889 (1978).
40. Krauch, T. et al. New base-pairs for DNA and RNA. In *Abstracts of Papers at the 196th ACS National Meeting of the American Chemical Society* (American Chemical Society, 1988).
41. Georgiadis, M. M. et al. Structural basis for a six nucleotide genetic alphabet. *J. Am. Chem. Soc.* **137**, 6947–6955 (2015).
42. Jimenez, R. M., Polanco, J. A. & Luptak, A. Chemistry and biology of self-cleaving ribozymes. *Trends Biochem. Sci.* **40**, 648–661 (2015).
43. Koo, S. C. et al. Transition state features in the hepatitis delta virus ribozyme reaction revealed by atomic perturbations. *J. Am. Chem. Soc.* **137**, 8973–8982 (2015).
44. Weinan, E., Liu, D. & Vanden-Eijnden, E. Nested stochastic simulation algorithm for chemical kinetic systems with disparate rates. *J. Chem. Phys.* **123**, 194107 (2005).
45. Vanden-Eijnden, E. & Venturoli, M. Revisiting the finite temperature string method for the calculation of reaction tubes and free energies. *J. Chem. Phys.* **130**, 194103 (2009).
46. Zamel, R. et al. Exceptionally fast self-cleavage by a *Neurospora* Varkud satellite ribozyme. *Proc. Natl Acad. Sci. USA* **101**, 1467–1472 (2004).
47. Mir, A. et al. Two divalent metal ions and conformational changes play roles in the hammerhead ribozyme cleavage reaction. *Biochemistry* **54**, 6369–6381 (2015).
48. Mir, A. & Golden, B. L. Two active site divalent ions in the crystal structure of the hammerhead ribozyme bound to a transition state analogue. *Biochemistry* **55**, 633–636 (2016).
49. Chen, H., Giese, T. J., Golden, B. L. & York, D. M. Divalent metal ion activation of a guanine general base in the hammerhead ribozyme: insights from molecular simulations. *Biochemistry* **56**, 2985–2994 (2017).
50. Gaines, C. S., Piccirilli, J. A. & York, D. M. The L-platform/L-scaffold framework: a blueprint for RNA-cleaving nucleic acid enzyme design. *RNA* <https://doi.org/10.1261/rna.071894.119> (2019).
51. Ward, W. L., Plakos, K. & DeRose, V. J. Nucleic acid catalysis: metals, nucleobases, and other cofactors. *Chem. Rev.* **114**, 4318–4342 (2014).
52. Anderson, M., Schultz, E. P., Martick, M. & Scott, W. G. Active-site monovalent cations revealed in a 1.55-Å-resolution hammerhead ribozyme structure. *J. Mol. Biol.* **425**, 3790–3798 (2013).
53. Rupert, P. B., Massey, A. P., Sigurdsson, S. T. & Ferre-D’Amare, A. R. Transition state stabilization by a catalytic RNA. *Science* **298**, 1421–1424 (2002).

**Publisher's note** Springer Nature remains neutral with regard to jurisdictional claims in published maps and institutional affiliations.

© The Author(s), under exclusive licence to Springer Nature Limited 2020

### Data availability

The data that support the findings of this study are available in the Supplementary Information file and from the corresponding authors upon request.

### Code availability

Simulation software are available in the latest release of AMBER18. Example input files, representative structures, animation of the active site in the presence and absence of the  $Mg^{2+}$  ion derived from the MD simulations and an animation of the catalytic reaction derived from the simulations are provided online free to download: <http://theory.rutgers.edu>.

### Acknowledgements

We thank S. DasGupta for valuable discussions. A.G., B.W., J.A.P. and D.M.Y. are grateful for the financial support provided by the National Institutes of Health (grant GM62248 to D.M.Y. and grant GM131568 to J.A.P.). B.P.W. acknowledges support from the Predoctoral Training Program in Chemistry and Biology (T32-GM008720). Computational resources were provided by the National Institutes of Health under grant no. S10OD012346, the Office of Advanced Research Computing (OARC) at Rutgers, the State University of New Jersey, Rutgers Discovery Information Institute (RDI<sup>2</sup>), the State University of New Jersey, and by the Extreme Science and Engineering Discovery Environment (XSEDE), which is supported by National Science Foundation grant no. OCI-1053575 (project no. TG-MCB110101). This research is also part of the Blue Waters sustained-petascale computing project, which is supported by the National Science

Foundation (awards OCI-0725070 and ACI-1238993) and the state of Illinois. Blue Waters is a joint effort of the University of Illinois at Urbana-Champaign and its National Center for Supercomputing Applications.

### Author contributions

A.G. and B.P.W. contributed equally to this work. A.G. performed the computations and B.P.W. performed the experiments. A.G., B.P.W., J.A.P. and D.M.Y. co-wrote the paper. T.J.G. developed enabling software and provided technical support to various aspects of the computational studies. N.-S.L. synthesized the phosphoramidites and oligonucleotides. S.H. and S.A.B. provided the hachimoji RNA substrate. S.R. characterized the stereochemistry of the phosphorothioate substrates. J.A.P. and D.M.Y. conceived and co-directed all experimental and computational aspects of the work.

### Competing interests

The authors declare no competing interests.

### Additional information

**Supplementary information** is available for this paper at <https://doi.org/10.1038/s41557-019-0391-x>.

**Correspondence and requests for materials** should be addressed to J.A.P. or D.M.Y.

**Reprints and permissions information** is available at [www.nature.com/reprints](http://www.nature.com/reprints).